Nano Research
2019, 12(7): 1613–1618

ISSN 1998-0124 CN 11-5974/O4
https://doi.org/10.1007/s12274-019-2400-1

Research Article

Defect engineering of molybdenum disulfide through ion irradiation to boost hydrogen evolution reaction performance

Cheng Sun[1,§], Peipei Wang[2,§], Hao Wang[1], Chuan Xu[2], Juntong Zhu[1], Yanxia Liang[2], Ying Su[1], Yining Jiang[1], Wenqi Wu[1], Engang Fu[2] (✉), and Guifu Zou[1] (✉)

[1] *Soochow Institute for Energy and Materials Innovations & Key Laboratory of Advanced Carbon Materials and Wearable Energy Technologies of Jiangsu Province, Soochow University, Suzhou 215006, China*
[2] *State Key Laboratory of Nuclear Physics and Technology, School of Physics, Peking University, Beijing 100871, China*
[§] *Cheng Sun and Peipei Wang contributed equally to this work.*

Received: 14 February 2019 / **Revised:** 22 March 2019 / **Accepted:** 1 April 2019

ABSTRACT

The inert basal plane of molybdenum disulfide (MoS_2) restrains its further hydrogen evolution reaction (HER) performance. This work attempts ion irradiation to activate inert basal plane of MoS_2 nanosheet to improve its electrocatalytic performance. Experimental results demonstrate the sulphur vacancies generated by ion irradiation on the basal plane of MoS_2 mainly boost the efficiency of HER performance. The moderate fluence of carbon ion irradiation gains the optimum HER performance with an onset potential of 77 mV and Tafel slope of 66 mV/dec.

KEYWORDS

MoS_2 nanosheet, ion irradiation, electrocatalyst, hydrogen evolution reaction, sulphur vacancy

1 Introduction

Hydrogen as a clean alternative to fossil fuels has attracted intense attentions. The electrocatalytic hydrogen evolution reaction is a reasonable approach to produce hydrogen [1–3]. Traditional hydrogen evolution reaction (HER) electrocatalysts including noble metal catalysts such as platinum-based catalysts show excellent catalytic performance. However, high price of noble materials has limited them for further applications [4, 5]. The transitional metal sulfides, represented by molybdenum disulfide, have attracted wide attention due to low cost, wide source, and the comparable catalytic properties of platinum-based catalysts [6–9]. MoS_2, as one HER catalyst, has been studied intensely for these years. It has three types of phases, which are 1T′-phase, 1T-phase and 2H-phase. Although 1T′-phase and 1T-phase MoS_2 with the features of metal phase have an excellent catalytic performance, their poor stability limits their application [10–13]. The 2H-phase MoS_2 is emerging to scientist's vision due to its good catalytic behavior and stability [6–13].

Many scientists attempted to enhance the catalytic performance of the materials such as MoS_2 by means of increasing the active sites according to the following three strategies: (1) morphology, in which the surface area of the materials is increased by developing different shapes of materials such as nanoparticles [9, 14], nanosheets [15], nanobelts [16]; (2) replacement, through which the heterogeneous atoms such as phosphorus [17], carbon [18, 19], tungsten [6], selenium [20], are doped to lower the hydrogen adsorption free energy to improve catalytic performance; (3) plasma treatment, in which argon plasma is used to produce sulfur vacancies on the basal plane and the edge of the MoS_2 [21, 22]. The above strategies are desirable to realize the increase of active sites for the efficient HER.

Researchers find that the edge active sites dominate the contribution of the electrocatalytic performance in MoS_2 [14, 22–24]. Accordingly, how to activate the inert basal plane of MoS_2 is an inspiring topic. As a powerful approach to modify the materials, ion irradiation has been widely used in aerospace, agriculture, industry and medical treatment due to its advantage of transferring high energy on the surface of materials [25, 26]. For example, the microstructure and properties of materials can be changed by ion irradiation [27, 28]. In this study, we propose to use the ion irradiation to create the active sites to improve the HER performance of MoS_2 for the first time. The study finds that sulphur vacancies as active sites dominate on the basal plane of MoS_2 to boost the efficient HER behavior. The tunable carbon ion (C^+) irradiation optimizes the HER catalytic performance with an onset potential of 77 mV and Tafel slope of 66 mV/dec.

2 Experimental section

2.1 Synthesis of MoS_2 samples

1T-phase MoS_2 nanosheets were prepared through a lithium intercalation and exfoliation method. First, the bulk MoS_2 was pre-expanded by refluxing in N_2H_4 at 130 °C for 24 h and then was lithiated in 1.6 M n-butyllithium in an Ar-filled dry box to form the lithium intercalated product (Li_xMoS_2). Then it was recovered by filtration and washed with hexane. Exfoliation was achieved by treating the Li_xMoS_2 with water under ultrasonication, then it was centrifuged at 2,000 rpm to remove unexfoliated crystals to form as-prepared MoS_2. The details can be found elsewhere [12]. C ion irradiation was performed on MoS_2 powder in NEC 1.7 MV Tandem accelerator at room temperature. Base pressure in the end-station

Address correspondence to Engang Fu, efu@pku.edu.cn; Guifu Zou, zouguifu@suda.edu.cn

during ion irradiation was less than 5×10^{-4} Pa. During the ion irradiation, the carbon ions were ionized from the ion source and then accelerated in the acceleration cavity with high-voltage electric field. Finally, the carbon ions passed through the target materials. The energy of C ion was 3 MeV, which would make sure that the incident ions (3 MeV C^+) pass entirely through the sample with almost no residual concentration. The total fluence for the samples is 5×10^{12}, 2×10^{13} and 5×10^{13} ions/cm^2, respectively.

2.2 Characterization

The microstructure of MoS_2 before and after irradiation was characterized by transmission electron microscopy (TEM), which was performed on a FEI Tecnai F30 microscope operating at 300 kV with a field-emission gun. X-ray diffraction (XRD) measurement was carried out on a D8 Advance (Bruker). X-ray photoelectron spectroscopy (XPS) was performed to study the chemical states of the as-prepared MoS_2 and the MoS_2 with different irradiation fluences on a Escalab 250Xi (Thermo Fisher). All the Raman spectra were collected using a confocal Raman spectrometre (Horiba, HR evolution) with an excitation wavelength of 633 nm. The electron spin resonance (ESR) spectra were performed with Elexsys E580 (Bruker) at room temperature. The range of microwave was set between 9.8591 and 9.8599 GHz, and the microwave power was set to 20 mW to prevent moisture and prevent oxidation.

2.3 Electrochemical measurements

The HER tests for different MoS_2 samples were carried out on a CHI 660E electrochemical workstation via a three-electrode electrochemical configuration in an N_2-purged 0.5 M H_2SO_4 electrolyte. The saturated Ag/AgCl was used as the reference electrode and the counter electrode was a graphite rod. All potentials were referenced to a reversible hydrogen electrode (RHE) according to E(vs. RHE) = E(vs. Ag/AgCl) + 0.21 + 0.059 × pH. The catalyst modified glassy carbon disk electrode was served as the working electrode. The catalyst suspension was prepared by dispersing 2 mg MoS_2 and 2 mg acetylene black in 250 μL solution containing 200 μL of ethanol and 50 μL of 5 wt.% Nafion with 30 min sonication. The 5 μL of this catalyst suspension was loaded onto a glassy carbon electrode (4 mm diameter, mass loading ~ 0.32 mg/cm^2). Linear scanning voltammetry was carried out with *IR* correction at a scan rate of 5 mV/s.

3 Results and discussion

Transmission electron microscope was used to characterize the microstructures of MoS_2 before and after ion irradiation. Figure 1(a) is the TEM image of as-prepared MoS_2 morphology and shows that the MoS_2 image has low contrast, indicating it is composed of few layers of MoS_2. Careful observation finds that there are some curling pieces of MoS_2 monolayer (marked with red ellipse in Fig. 1(a)) in the specimen. Figure 1(b) is the high resolution TEM (HRTEM) image of as-prepared MoS_2 and shows its microstructure at atomic scale. As-prepared MoS_2 has single crystalline structure and the interplanar spacing is measured to be 0.27 nm, corresponding to the d spacing of MoS_2 (100) planes. The corresponding fast Fourier transform (FFT) pattern shown in the inset of Fig. 1(b) clearly exhibits six diffraction spots, indicating the hexagonal structure. Figure 1(b1) shows the processed image by applying mask of (100) planes and it is defect-free before ion irradiation.

Figure 1(c) shows the HRTEM image of the ion-irradiated MoS_2 by 3 MeV C ions with a total fluence of 5×10^{12} ions/cm^2 (denoted as MoS_2-irra1). The area circled by magenta dashed circle shows a relatively disordered atomic arrangement, which may result in some crack and the formation of additional edges. The processed image (Fig. 1(c1)) by applying mask of (100) planes reveals that dislocation (labelled by red mark) is formed in the MoS_2 nanosheet.

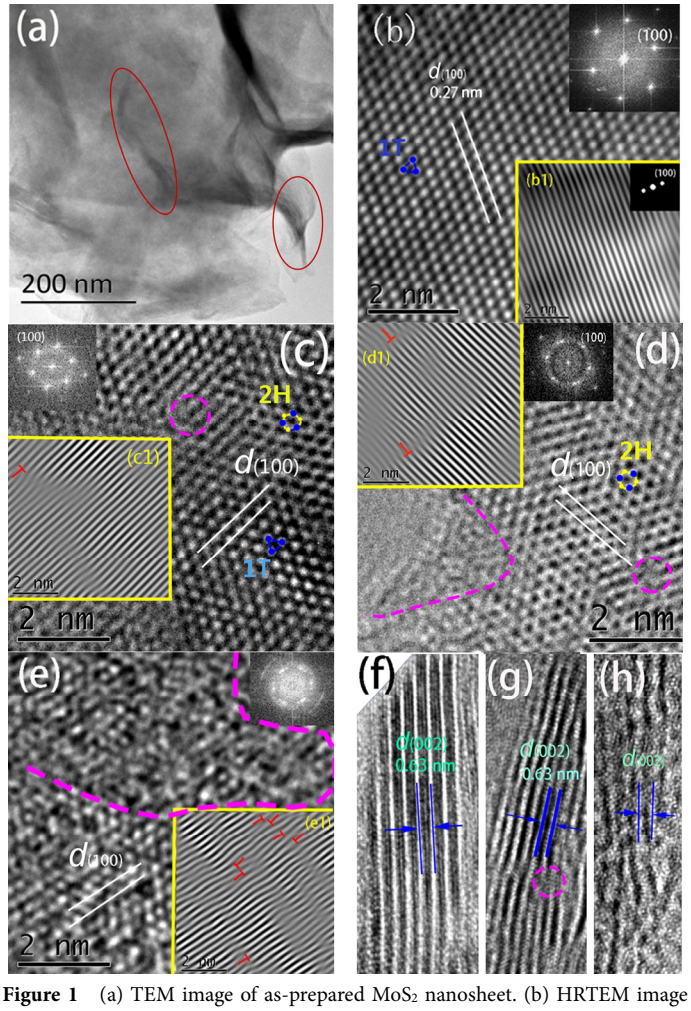

Figure 1 (a) TEM image of as-prepared MoS_2 nanosheet. (b) HRTEM image and the corresponding fast Fourier transform pattern of as-prepared MoS_2 nanosheet. (c)–(e) HRTEM images of ion-irradiated MoS_2 nanosheets with the fluences of 5×10^{12} cm^{-2} (MoS_2-irra1), 2×10^{13} cm^{-2} (MoS_2-irra2) and 5×10^{13} cm^{-2} (MoS_2-irra3). (f)–(h) the typical lamellar structure within MoS_2-irra1, MoS_2-irra2 and MoS_2-irra3 nanosheets. The red "T" represents dislocation and areas surrounded by magenta dashed curve represent disordered regions. The blue and yellow sphere structures represent molybdenum and sulfur atoms, respectively.

It implies the occurrence of the sulfur vacancy on the basal plane of ion-irradiated MoS_2 nanosheets. Figures 1(d) and 1(e) are the HRTEM images of MoS_2 nanosheets further irradiated by 3 MeV C ions with a total fluence of 2×10^{13} ions/cm^2 (denoted as MoS_2-irra2) and 5×10^{13} ions/cm^2 (denoted as MoS_2-irra3), respectively. The increasing disorder area (curved by magenta dashed lines) and dislocations (red marks) inside the MoS_2 nanosheet are observed. The corresponding FFT patterns in the insets of Figs. 1(d) and 1(e) show six independent diffraction arcs, confirming the defect-rich quasiperiodic structure of the ion-irradiated MoS_2.

The typical lamellar structure with interlayer spacing of 0.63 nm can be observed from the HRTEM image of the ion-irradiated MoS_2 nanosheets (Figs. 1(f)–1(h)). It is noted that the crystalline lattice has been partly destroyed with the heavy ion irradiation. Particularly, the existence of rich defects is revealed by the discontinuous crystal fringes along the curled edge in higher irradiation dose (Figs. 1(g) and 1(h)). Furthermore, these HRTEM images and FFT patterns reveal the phase transition from 1T to 2H in the ion-irradiated MoS_2 samples with distinct atomic arrangements shown in Figs. 1(c) and 1(d). This phase transition is controllable through the fluence of ion irradiation.

Figure 2(a) shows XPS spectra of as-prepared MoS_2 and ion-irradiated MoS_2 with radiation fluence of 2×10^{13} ions/cm^2 (MoS_2-

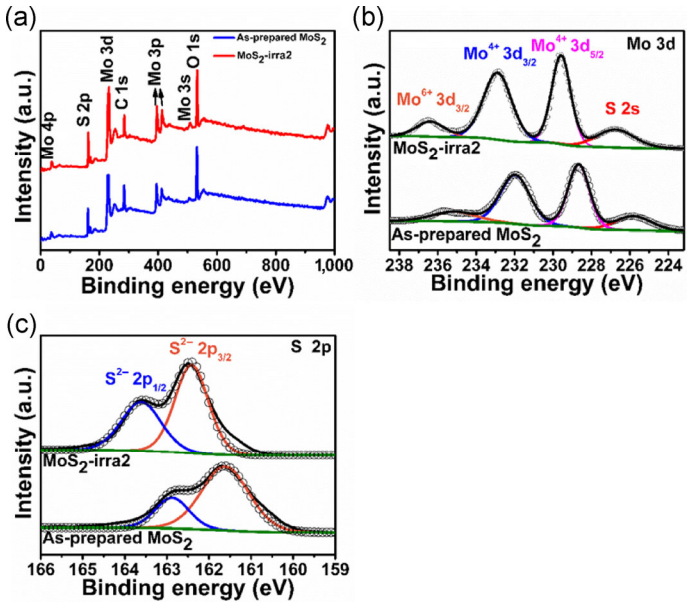

Figure 2 (a) XPS survey spectra, (b) Mo 3d and (c) S 2p of as-prepared MoS_2 and MoS_2-irra2.

irra2). Both of the XPS scans present the similar data indexed to be elements of Mo, S and part of C and O in the samples. Figure 2(b) shows two characteristic peaks of Mo $3d_{5/2}$ and Mo $3d_{3/2}$ orbitals, located at 228.7 and 231.9 eV in as-prepared MoS_2, as well as 229.6 and 232.9 eV in MoS_2-irra2, suggesting the dominance of Mo^{IV} in both samples. Besides, we can obviously observe that the ion irradiation induces the phase of MoS_2 from 1T to 2H since the position of the peak shifts to the left for about 0.9 eV as the previous literature reported [10]. The conclusion of phase transition was also confirmed by the Raman spectra of as-prepared MoS_2 and ion-irradiated MoS_2 shown in Figs. S1(a) and S1(b) in the Electronic Supplementary Material (ESM). Several specific peaks of 1T phase in the region of J_1 disappear after ion irradiation, which implies the occurrence of phase transition according to Eda and co-workers' study [29]. Significantly, we find that MoS_2-irra1 shown in Fig. S2 in the ESM is composed of 1T phase and 2H phase and MoS_2-irra3 has 2H phase. The phase transform was induced by ion irradiation [30]. Simultaneously, Fig. 2(c) shows that the spectra of sulfur exhibit a single doublet with the $2p_{3/2}$ peak located at 162.9 and 161.6 eV in as-prepared MoS_2, 163.6 and 162.4 eV in MoS_2-irra2, respectively. All these can be indexed to −2 valence states of sulphur, confirming the MoS_2 structure. Compositional analysis of MoS_2 before and after ion irradiation (MoS_2-irra2) can be estimated to be Mo/S atomic ratio of 1:1.76 and 1:1.54, respectively. The obvious decrease of sulfur atom ratio means sulfur vacancies occurrence in the sample with irradiation [31]. Commonly, the increase of sulfur vacancies may increase the HER performance of the relative sample. Besides, the envelope of S 2p spectrum of MoS_2-irra2 shows that there are some amorphous molybdenum sulfides in the sample [29], which is consistent with the result from HRTEM.

According to the experimental analyses, we schematize the whole structure evolution of MoS_2 sample subjected to ion irradiation in Fig. 3. Firstly, the highly crystalline bulk MoS_2 was chemically exfoliated to transfer from multilayered 2H phase MoS_2 to few-layered 1T phase MoS_2. Secondly, the samples of 1T phase MoS_2 were irradiated with different ion fluences. When the ion fluence is low, the microstructure was transformed from single crystalline 1T phase to partial 2H phase with polycrystalline and rare amorphous regions (MoS_2-irra1). Radiation causes plenty of point defects such as sulphur vacancies (marked in red circle) on the basal plane of MoS_2, which generate many dislocations and sub-grain boundaries [32].

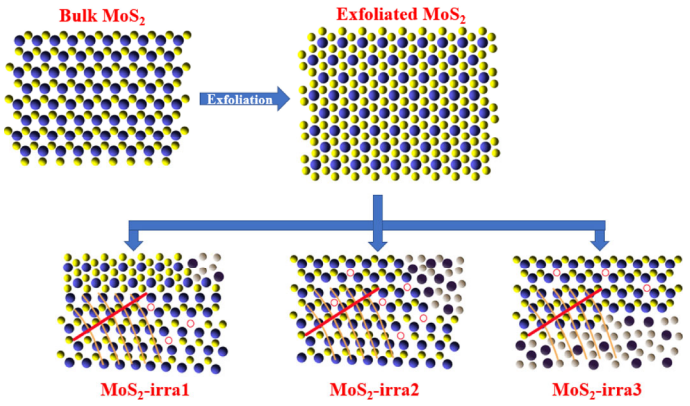

Figure 3 The schematic diagram of MoS_2 structure evolution by controlling the C ion fluences. The blue is molybdenum, yellow is sulfur, purple is amorphous molybdenum and grey is amorphous sulfur.

Thirdly, more amorphous regions and sulphur vacancies appear with the increase of ion fluence to 2×10^{13} ions/cm^2 (MoS_2-irra2). This moderate defect distribution will activate the basal plane of MoS_2 and would no doubt enhance its HER performance. It is noting that, nearly all 1T phase MoS_2 turns into 2H phase at this stage, which largely improves the stability of MoS_2. Finally, the further increase dose of ion fluence to 5×10^{13} ions/cm^2 (MoS_2-irra3) will produce quantities of amorphous regions. This might deteriorate the HER performance of MoS_2. All these will be demonstrated in the following HER measurements.

Figure 4 displays the polarization curves and the corresponding Tafel plots of the different MoS_2 samples for HER. The kinetics of HER can be illustrated by the relationship between the overpotential and current density. Therefore, each plot was obtained according to the simplified Tafel equation ($\eta = b\log j + a$), η is the overpotential, j is the current density, a and b are the constants of the Tafel equation, especially, b is defined as Tafel slope. The lower the Tafel slope is, the lower the overpotential is required to achieve the same current density and the higher the catalytic activity is. As seen from Figs. 4(a) and 4(b), the catalytic performance of the exfoliated MoS_2 (as-prepared MoS_2) is much better than that of the bulk MoS_2. The result can be attributed to the two-electron transfer process of 1T

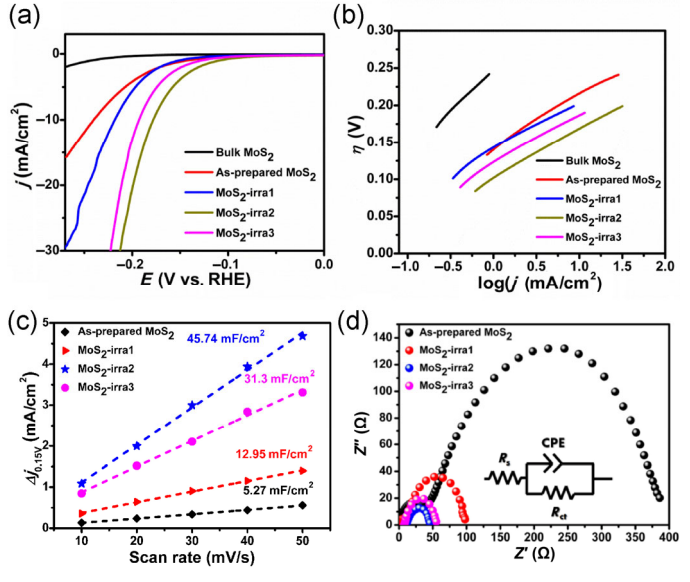

Figure 4 (a) Polarization curves and (b) corresponding Tafel slope of bulk MoS_2, as-prepared MoS_2 and ion-irradiated MoS_2 with fluence of 5×10^{12} cm^{-2}, 2×10^{13} cm^{-2} and 5×10^{13} cm^{-2}; (c) the extracted double-layer capacitances of these samples using a cyclic voltammetry method; (d) EIS Nyquist plots recorded on different irradiation fluences with the potential of −0.423 V set at −0.2 V vs. RHE. Inset is the equivalent circuit.

MoS_2. The similar phenomenon has been reported in the previous literatures [12, 33]. It is worthy of noting that all of the MoS_2 specimens irradiated with different fluences have better HER performance than that of the exfoliated MoS_2. The increase of active sites after ion irradiation could mainly contribute to the better HER performance. The radiation induced defects including sulfur vacancies involve the formation of more active sites in the irradiated MoS_2 samples. On one hand, the generated sulphur vacancies and amorphous on the basal plane of MoS_2 could increase more active sites to improve catalytic performance [6, 34], on the other hand, multi-layered structure and phase transition restrain the HER performance inversely [35]. Therefore, there should be a tunable irradiation fluence to obtain an optimal hydrogen evolution performance. Figures 4(a) and 4(b) illustrate the best catalytic performance of MoS_2-irra2 with an onset potential of 77 mV and Tafel slope of 66 mV/dec. Furthermore, this catalytic performance is comparable to the previous reports of MoS_2 and its derivatives with different treatments (Table 1) [9, 22, 31, 36–38]. The results conform to the microstructure evolution and the balance between sulfur vacancy and amorphous. To study the redox stability of MoS_2-irra2, its polarization curves were measured again after it swept for 4,000 circles in cyclic voltammetry shown in Fig. S3 in the ESM. The results show that its HER performance has declined by 12.4% and maintained a polarization curve similar to the initial one [39].

To further explore the mechanism of the irradiated MoS_2 catalytic behavior, we performed cyclic voltammogrametry measurement to obtain the double-layer capacitance (C_{dl}), which is proportional to the effective electrochemically active surface area (ECSA). The C_{dl} of these samples are investigated in 0.5 M H_2SO_4 to provide a relative comparison (Fig. S4 in the ESM). Capacitive current is plotted as a function of scan rate to extract the C_{dl} (Fig. 4(c)), whose slope is equivalent to twice the value of C_{dl} [40]. The C_{dl} values are calculated to be 45.74, 31.3, 12.95 and 5.27 mF/C^2 for MoS_2-irra2, MoS_2-irra3, MoS_2-irra1 and as-prepared MoS_2, respectively. The data illustrate that the MoS_2-irra2 has the highest exposure of catalytic active sites. Compared with MoS_2-irra2, MoS_2-irra1 shows less active sites from amorphous MoS_2 and sulphur vacancies. Nevertheless, there are more amorphous states than sulphur vacancies in MoS_2-irra3. Therefore, MoS_2-irra2 presents the best HER performance in this study. The ECSA is reduced in comparison between MoS_2-irra3 and MoS_2-irra2 after further irradiation, indicating that the excess amorphous MoS_2 phase may restrain the further improvement of HER performance since excess amorphous MoS_2 may contribute to reduced surface area and conductivity according to previous literatures [13, 39, 40].

Besides, Fig. 4(d) shows the fitting of the Nyquist plot of MoS_2 catalysts which was obtained by the electrochemical impedance spectroscopy (EIS) measurement. The inset equivalent electric circuit is an important model for the solid–liquid interface. The constant phase element (CPE) was employed when fitting the plot.

Table 1 Comparison of HER performance of MoS_2 and other reported catalysis

Catalysts	Onset potential η (mV)	Tafel slope (mV/dec)	Mass loading (mg/cm^2)	η (mV) at current density of 10 mA/cm^2	References
MoS_2/RGO	~ 80	41	0.28	~ 150	[9]
MoS_2	70	60	—	170	[22]
MoS_2	~ 180	—	—	620	[31]
MoS_2	~ 95	46	0.28	160	[36]
MoS_2	~ 400	104	—	520	[37]
Co/MoS_2	~ 70	82	—	210	[38]
This work	77	66	~ 0.32	177	

The R_s means the resistance of the solution and it is overpotential independent about 8.5 Ω. From this impedance data, we can get the charge transfer resistance (R_{ct}) of each sample, which is ~ 350, ~ 100, ~ 45 and ~ 65 Ω for the as-prepared MoS_2, MoS_2-irra1, MoS_2-irra2 and MoS_2-irra3, respectively. The R_{ct} is inversely proportional to the hydrogen evolution reaction rate. The bigger the semi-circular arc is, the larger the impedance is. Consequently, the MoS_2 catalysts with lower R_{ct} always exhibit a lower interface reaction and better performance [41]. It is clearly revealed that the R_{ct} of the sample MoS_2-irra2 has the smallest value of impedance, implying its efficient charge transfer. This phenomenon agrees well with the low Tafel slopes in Fig. 4(b). This is reasonable since moderate irradiation may make more Mo atoms expose to enhance its conductivity while both of a small quantity of irradiation and excess irradiation (i.e., MoS_2-irra1 and MoS_2-irra3) can cause the reduction of conductivity due to the reduction exposure of Mo atoms.

Further insight into the existence and production of sulfur vacancy on the basal plane of MoS_2 with different irradiation fluences, we obtained the fingerprint information for a paramagnetic signal from electron spin resonance spectra. The sulphur signal was achieved at ~ 3,330 G which reflects the intensity of Mo–S dangling bonds according to the previous reports [12, 42]. A lower intensity of sulphur signal indicates higher concentration of sulphur vacancies. We may conclude that the lower intensity of Mo–S dangling bonds means the existence of sulfur vacancy as well as the more sulfur vacancies. As it can be seen from Fig. 5, the bulk MoS_2 and exfoliated MoS_2 show negligible sulphur signal due to the excellent crystallinity and purity. To one's excitement, the ESR intensities of irradiated MoS_2 samples were 4.9, 6.5 and 13.2 a.u./mg for MoS_2-irra2, MoS_2-irra3 and MoS_2-irra1, respectively. It gives a strong support to address that our ion irradiation method is feasible to introduce the sulphur vacancies in the MoS_2 samples. It is a very significant evidence to design the desirable vacancy for the other materials.

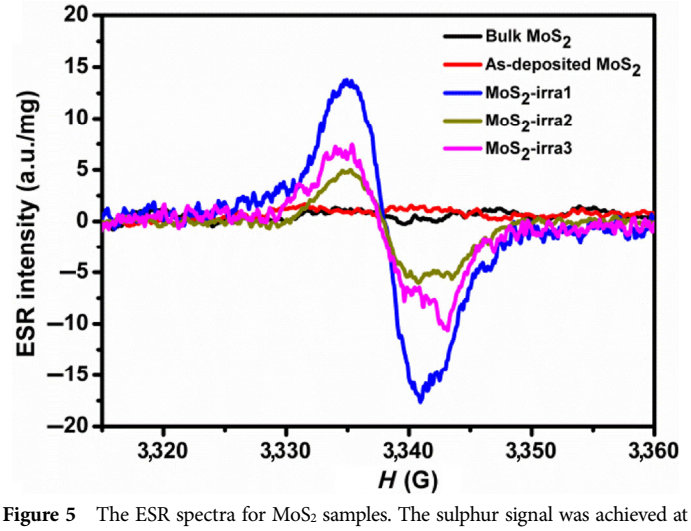

Figure 5 The ESR spectra for MoS_2 samples. The sulphur signal was achieved at ~ 3,330 G and a lower intensity of sulphur signal indicates higher concentration of sulphur vacancies.

4 Conclusions

The tunable sulphur vacancy is well introduced to the basal plane of MoS_2 by ion irradiation. It is found that the ion fluence plays a major role in improving the HER performance of MoS_2. The different ion fluences can tune the number of the sulphur vacancy and amorphous phase on the basal plane of MoS_2. The ion-irradiated MoS_2 upon the fluence of 2×10^{13} ions/cm^2 exhibits the best HER performance with an onset potential of 77 mV and Tafel slope of 66 mV/dec. The experiments demonstrate more active sites caused by sulphur vacancies from the basal plane mainly contribute to higher HER cata-

lytic efficiency while more amorphous state restricts the performance of MoS_2. This effective and feasible approach of ion irradiation provides a platform to introduce the desirable vacancy for the other similar materials.

Acknowledgements

We gratefully acknowledge the support from the National Natural Science Foundation of China (Nos. 21671141, 11375018 and 11528508), the National Basic Research Program of China (No. 2015CB358600), the Priority Academic Program Development (PAPD) of Jiangsu Higher Education Institutions for Optical Engineering in Soochow University, the National Magnetic Confinement Fusion Energy Research Project (Nos. 2015GB121004, 2017YFE0302500 and 2018YFE0307100) from Ministry of Science and Technology of China, China-Romania Science and Technology Cooperation committee 43rd Regular Meeting Exchange program and Ion Beam Materials Laboratory (IBML) at Peking University.

Electronic Supplementary Material: Supplementary material (Raman spectra and CV curves at different scan rates of all these samples, XPS spectra of MoS_2-irra1 and MoS_2-irra3, and polarization of the MoS_2-irra2 before and after 4,000 circles of CV) is available in the online version of this article at https://doi.org/10.1007/s12274-019-2400-1.

References

[1] Chu, S.; Majumdar, A. Opportunities and challenges for a sustainable energy future. *Nature* **2012**, *488*, 294–303.

[2] Wang, H.; Gao, L. J. Recent developments in electrochemical hydrogen evolution reaction. *Curr. Opin. Electrochem.* **2018**, *7*, 7–14.

[3] Chou, S. W.; Lai, Y. R.; Yang, Y. Y.; Tang, C. Y.; Hayashi, M.; Chen, H. C.; Chen, H. L.; Chou, P. T. Uniform size and composition tuning of PtNi octahedra for systematic studies of oxygen reduction reactions. *J. Catal.* **2014**, *309*, 343–350.

[4] Casado-Rivera, E.; Volpe, D. J.; Alden, L.; Lind, C.; Downie, C.; Vázquez-Alvarez, T.; Angelo, A. C. D.; DiSalvo, F. J.; Abruña, H. D. Electrocatalytic activity of ordered intermetallic phases for fuel cell applications. *J. Am. Chem. Soc.* **2004**, *126*, 4043–4049.

[5] Greeley, J.; Jaramillo, T. F.; Bonde, J.; Chorkendorff, I.; Nørskov, J. K. Computational high-throughput screening of electrocatalytic materials for hydrogen evolution. *Nat. Mater.* **2006**, *5*, 909–913.

[6] Merki, D.; Hu, X. L. Recent developments of molybdenum and tungsten sulfides as hydrogen evolution catalysts. *Energy Environ. Sci.* **2011**, *4*, 3878–3888.

[7] Lu, Q. P.; Yu, Y. F.; Ma, Q. L.; Chen, B.; Zhang, H. 2D Transition-metal-dichalcogenide-nanosheet-based composites for photocatalytic and electrocatalytic hydrogen evolution reactions. *Adv. Mater.* **2016**, *28*, 1917–1933.

[8] Wang, H.; Ouyang, L. Y.; Zou, G. F.; Sun, C.; Hu, J.; Xiao, X.; Gao, L. J. Optimizing MoS_2 edges by alloying isovalent W for robust hydrogen evolution activity. *ACS Catal.* **2018**, *8*, 9529–9536.

[9] Li, Y. G.; Wang, H. L.; Xie, L. M.; Liang, Y. Y.; Hong, G. S.; Dai, H. J. MoS_2 nanoparticles grown on graphene: An advanced catalyst for the hydrogen evolution reaction. *J. Am. Chem. Soc.* **2011**, *133*, 7296–7299.

[10] Voiry, D.; Mohite, A.; Chhowalla, M. Phase engineering of transition metal dichalcogenides. *Chem. Soc. Rev.* **2015**, *44*, 2702–2712.

[11] Eda, G.; Fujita, T.; Yamaguchi, H.; Voiry, D.; Chen, M. W.; Chhowalla, M. Coherent atomic and electronic heterostructures of single-layer MoS_2. *ACS Nano* **2012**, *6*, 7311–7317.

[12] Yin, Y.; Han, J. C.; Zhang, Y. M.; Zhang, X. H.; Xu, P.; Yuan, Q.; Samad, L.; Wang, X. J.; Wang, Y.; Zhang, Z. H. et al. Contributions of phase, sulfur vacancies, and edges to the hydrogen evolution reaction catalytic activity of porous molybdenum disulfide nanosheets. *J. Am. Chem. Soc.* **2016**, *138*, 7965–7972.

[13] Yan, Y.; Xia, B. Y.; Xu, Z. C.; Wang, X. Recent development of molybdenum sulfides as advanced electrocatalysts for hydrogen evolution reaction. *ACS Catal.* **2014**, *4*, 1693–1705.

[14] Benson, J.; Li, M. X.; Wang, S. B.; Wang, P.; Papakonstantinou, P. Electrocatalytic hydrogen evolution reaction on edges of a few layer molybdenum disulfide nanodots. *ACS Appl. Mater. Interfaces* **2015**, *7*, 14113–14122.

[15] Huang, X.; Zeng, Z. Y.; Bao, S. Y.; Wang, M. F.; Qi, X. Y.; Fan, Z. X.; Zhang, H. Solution-phase epitaxial growth of noble metal nanostructures on dispersible single-layer molybdenum disulfide nanosheets. *Nat. Commun.* **2013**, *4*, 1444.

[16] Yang, L.; Hong, H.; Fu, Q.; Huang, Y. F.; Zhang, J. Y.; Cui, X. D.; Fan, Z. Y.; Liu, K. H.; Xiang, B. Single-crystal atomic-layered molybdenum disulfide nanobelts with high surface activity. *ACS Nano* **2015**, *9*, 6478–6483.

[17] Huang, J. W.; Li, Y. R.; Xia, Y. F.; Zhu, J. T.; Yi, Q. H.; Wang, H.; Xiong, J.; Sun, Y. H.; Zou, G. F. Flexible cobalt phosphide network electrocatalyst for hydrogen evolution at all pH values. *Nano Res.* **2017**, *10*, 1010–1020.

[18] Wang, H.; Cao, Y. J.; Sun, C.; Zou, G. F.; Huang, J. W.; Kuai, X. X.; Zhao, J. Q.; Gao, L. J. Strongly coupled molybdenum carbide on carbon sheets as a bifunctional electrocatalyst for overall water splitting. *ChemSusChem* **2017**, *10*, 3540–3546.

[19] Wang, H.; Sun, C.; Cao, Y. J.; Zhu, J. T.; Chen, Y.; Guo, J.; Zhao, J.; Sun, Y. H.; Zou, G. F. Molybdenum carbide nanoparticles embedded in nitrogen-doped porous carbon nanofibers as a dual catalyst for hydrogen evolution and oxygen reduction reactions. *Carbon* **2017**, *114*, 628–634.

[20] Xia, Y. F.; Huang, J. W.; Wu, W. Q.; Zhang, Y. D.; Wang, H.; Zhu, J. T.; Yao, J. J.; Xu, L.; Sun, Y. H.; Zhang, L. et al. Sulfur-doped rhenium selenide vertical nanosheets: A high-performance electrocatalyst for hydrogen evolution. *ChemCatChem* **2018**, *10*, 4424–4430.

[21] Liu, H. W.; Liang, S. P.; Wu, T. J.; Chang, H. M.; Kao, P. K.; Hsu, C. C.; Chen, J. Z.; Chou, P. T.; Cheng, I. C. Rapid atmospheric pressure plasma jet processed reduced graphene oxide counter electrodes for dye-sensitized solar cells. *ACS Appl. Mater. Interfaces* **2014**, *6*, 15105–15112.

[22] Li, H.; Tsai, C.; Koh, A. L.; Cai, L. L.; Contryman, A. W.; Contryman, A. H.; Zhao, J. H.; Han, H. S.; Manoharan, H. C.; Abild-Pedersen, F. et al. Activating and optimizing MoS_2 basal planes for hydrogen evolution through the formation of strained sulphur vacancies. *Nat. Mater.* **2016**, *15*, 48–53.

[23] Voiry, D.; Salehi, M.; Silva, R.; Fujita, T.; Chen, M. W.; Asefa, T.; Shenoy, V. B.; Eda, G.; Chhowalla, M. Conducting MoS_2 nanosheets as catalysts for hydrogen evolution reaction. *Nano Lett.* **2013**, *13*, 6222–6227.

[24] Hinnemann, B.; Moses, P. G.; Bonde, J.; Jorgensen, K. P.; Nielsen, J. H.; Horch, S.; Chorkendorff, I.; Norskov, J. K. Biomimetic hydrogen evolution: MoS_2 nanoparticles as catalyst for hydrogen evolution. *J. Am. Chem. Soc.* **2005**, *127*, 5308–5309.

[25] Gómez-Navarro, C.; De Pablo, P. J.; Gómez-Herrero, J.; Biel, B.; Garcia-Vidal, F. J.; Rubio, A.; Flores, F. Tuning the conductance of single-walled carbon nanotubes by ion irradiation in the Anderson localization regime. *Nat. Mater.* **2005**, *4*, 534–539.

[26] Ogata, T.; Teshima, T.; Inaoka, M.; Minami, K.; Tsuchiya, T.; Isono, M.; Furusawa, Y.; Matsuura, N. Carbon ion irradiation suppresses metastatic potential of human non-small cell lung cancer A549 cells through the phosphatidylinositol-3-kinase/Akt signaling pathway. *J. Radiat. Res.* **2011**, *52*, 374–379.

[27] Wang, Z. X.; Yu, L. P.; Zhang, W.; Ding, Y. F.; Li, Y. L.; Han, J. G.; Zhu, Z. Y.; Xu, H. J.; He, G. W.; Chen, Y.; Hu, G. Amorphous molecular junctions produced by ion irradiation on carbon nanotubes. *Phys. Lett. A* **2004**, *324*, 321–325.

[28] Sun, Y. J.; Liang, Y. X.; Luo, M. C.; Lv, F.; Qin, Y. N.; Wang, L.; Xu, C.; Fu, E. G.; Gu, S. J. Defects and interfaces on PtPb nanoplates boost fuel cell electrocatalysis. *Small* **2018**, *14*, 1702259.

[29] Eda, G.; Yamaguchi, H.; Voiry, D.; Fujita, T.; Chen, M. W.; Chhowalla, M. Photoluminescence from chemically exfoliated MoS_2. *Nano Lett.* **2011**, *11*, 5111–5116.

[30] Kappera, R.; Voiry, D.; Yalcin, S. E.; Branch, B.; Gupta, G.; Mohite, A. D.; Chhowalla, M. Phase-engineered low-resistance contacts for ultrathin MoS_2 transistors. *Nat. Mater.* **2014**, *13*, 1128–1134.

[31] Chen, Y.; Huang, S. X.; Ji, X.; Adepall, K.; Yin, K. D.; Ling, X.; Wang, X. W.; Xue, J. M.; Dresselhaus, M.; Kong, J. et al. Tuning electronic structure of single layer MoS_2 through defect and interface engineering. *ACS Nano* **2018**, *12*, 2569–2579.

[32] Hansen, N.; Huang, X. Microstructure and flow stress of polycrystals and single crystals. *Acta Mater.* **1998**, *46*, 1827–1836.

[33] Conway, B. E.; Tilak, B. V. Interfacial processes involving electrocatalytic evolution and oxidation of H_2, and the role of chemisorbed H. *Electrochim. Acta* **2002**, *47*, 3571–3594.

[34] Chang, Y. H.; Lin, C. T.; Chen, T. Y.; Hsu, C. L.; Lee, Y. H.; Zhang, W. J.; Wei, K. H.; Li, L. J. Highly efficient electrocatalytic hydrogen production by MoS_x grown on graphene-protected 3D Ni foams. *Adv. Mater.* **2013**, *25*, 756–760.

[35] Yu, Y. F.; Huang, S. Y.; Li, Y. P.; Steinmann, S. N.; Yang, W. T.; Cao, L. Y. Layer-dependent electrocatalysis of MoS_2 for hydrogen evolution. *Nano Lett.* **2014**, *14*, 553–558.

[36] Li, Y.; Yin, K.; Wang, L. L.; Lu, X. L.; Zhang, Y. Q.; Liu, Y. T.; Yan, D. F.; Song, Y. Z.; Luo, S. L. Engineering MoS_2 nanomesh with holes and lattice defects for highly active hydrogen evolution reaction. *Appl. Catal. B: Environ.* **2018**, *239*, 537–544.

[37] Madauß, L.; Zegkinoglou, I.; Muiños, H. V.; Choi, Y. W.; Kunze, S.; Zhao, M. Q.; Naylor, C. H.; Ernst, P.; Pollmann, E.; Ochedowski, O. et al. Highly active single-layer MoS_2 catalysts synthesized by swift heavy ion irradiation. *Nanoscale* **2018**, *10*, 22908–22916.

[38] Park, S.; Park, J.; Abroshan, H.; Zhang, L.; Kim, J. K.; Zhang, J. M.; Guo, J. H.; Siahrostami, S.; Zheng, X. L. Enhancing catalytic activity of MoS_2 basal plane S-vacancy by Co cluster addition. *ACS Energy Lett.* **2018**, *3*, 2685–2693.

[39] Yan, Y.; Ge, X. M.; Liu, Z. L.; Wang, J. Y.; Lee, J. M.; Wang, X. Facile synthesis of low crystalline MoS_2 nanosheet-coated CNTs for enhanced hydrogen evolution reaction. *Nanoscale* **2013**, *5*, 7768–7771.

[40] Merki, D.; Vrubel, H.; Rovelli, L.; Fierro, S.; Hu, X. L. Fe, Co, and Ni ions promote the catalytic activity of amorphous molybdenum sulfide films for hydrogen evolution. *Chem. Sci.* **2012**, *3*, 2515–2525.

[41] Huang, J. W.; Sun, Y. H.; Zhang, Y. D.; Zou, G. F.; Yan, C. Y.; Cong, S.; Lei, T. Y.; Dai, X.; Guo, J.; Lu, R. F. et al. A new member of electrocatalysts based on nickel metaphosphate nanocrystals for efficient water oxidation. *Adv. Mater.* **2018**, *30*, 1705045.

[42] González, J. R.; Alcántara, R.; Tirado, J. L.; Fielding, A. J.; Dryfe, R. A. W. Electrochemical interaction of few-layer molybdenum disulfide composites vs sodium: New insights on the reaction mechanism. *Chem. Mater.* **2017**, *29*, 5886–5895.